Background radiation in inelastic X-ray scattering and X-ray emission spectroscopy. A study for Johann-type spectrometers

O.A. Paredes Mellone [a,b,*], L.M. Bianco [a,b], S.A. Ceppi [a,b], M. Goncalves Honnicke [c], G.E. Stutz [a,b]

[a] *Facultad de Matemática, Astronomía, Física y Computación (FaMAF), Universidad Nacional de Córdoba (UNC), 5000 Córdoba, Argentina*
[b] *IFEG, CONICET–UNC, FaMAF, 5000 Córdoba, Argentina*
[c] *Instituto de Ciencias da Vida e da Natureza, Universidade Federal da Integracao Latino-Americana, 2044, Foz do Iguacu, Parana 85867-970, Brazil*

ABSTRACT

A study of the background radiation in inelastic X-ray scattering (IXS) and X-ray emission spectroscopy (XES) based on an analytical model is presented. The calculation model considers spurious radiation originated from elastic and inelastic scattering processes along the beam paths of a Johann-type spectrometer. The dependence of the background radiation intensity on the medium of the beam paths (air and helium), analysed energy and radius of the Rowland circle was studied. The present study shows that both for IXS and XES experiments the background radiation is dominated by spurious radiation owing to scattering processes along the sample-analyser beam path. For IXS experiments the spectral distribution of the main component of the background radiation shows a weak linear dependence on the energy for the most cases. In the case of XES, a strong non-linear behaviour of the background radiation intensity was predicted for energy analysis very close to the backdiffraction condition, with a rapid increase in intensity as the analyser Bragg angle approaches $\pi/2$. The contribution of the analyser–detector beam path is significantly weaker and resembles the spectral distribution of the measured spectra. Present results show that for usual experimental conditions no appreciable structures are introduced by the background radiation into the measured spectra, both in IXS and XES experiments. The usefulness of properly calculating the background profile is demonstrated in a background subtraction procedure for a real experimental situation. The calculation model was able to simulate with high accuracy the energy dependence of the background radiation intensity measured in a particular XES experiment with air beam paths.

1. Introduction

With the advent of high-brilliance tunable X-ray sources, as third generation synchrotrons, many spectroscopic techniques have benefited from the possibility of performing high energy resolution experiments along with a high photon flux. Among them, inelastic X-ray scattering spectroscopy (IXS) is nowadays a well-established technique for investigating core and valence electron excitations on a variety of systems [1]. In particular, unique field of IXS using hard X-rays is the study of bulk electronic structure and excitations of systems under extreme conditions [2–4]. In a like manner, X-ray emission spectroscopy has emerged as a powerful element-specific technique to probe the electronic structure of the emitting atom and also its dependence on the chemical environment, having been mainly applied to 3d transition metal complexes [5–7]. Furthermore, in the field of the fundamental atomic physics, high resolution XES measurements can provide valuable

information to support newly developed theoretical approaches to calculate atomic structure and to simulate satellite spectra following shake processes [8–10]. Such IXS and XES studies are strongly demanding for high energy resolution. This requirement is usually achieved by means of a Johann-type spectrometer using nearly backdiffracting crystals for the energy analysis of the scattered or fluorescence X-ray photons, according to the kind of experiment.

A precise data processing in X-ray spectroscopy is generally a challenging task. Besides usual energy-dependent corrections, as absorption of the incident and outgoing beam in the sample, scale factors, reflectivity of the analyser crystal, etc., which are required to be applied depending on the type of experiment one is concerned with, the subtraction of spurious spectral components may demand attention. Among them, the background radiation owing to spurious radiation and the contribution from multiple scattering processes occurring in the sample are the most

---

commonly taken into account. An incorrect modelling of these spectral components may lead to misleading results, in particular in experiments intended to investigate weak spectral features in IXS or XES spectra. Several works have been devoted to propose procedures for data analysis and for experiment planning, particularly in the field of IXS [11–13]. The influence of multiple scattering on the IXS spectrum was also investigated using a Monte Carlo code [14]. That study demonstrated that under conditions realised in experiments, the double scattering contribution to the valence electron part of the spectrum is at most ~4% and that no additional structure into the IXS spectra of simple metals is introduced by multiple scattering effects.

Usually, in a first approximation, the spectral distribution of the background radiation is assumed to be constant or, in some cases, simulated by a linear function. However, a detailed analysis of the different spectral components of an XES spectrum revealed a non-linear behaviour of the intensity distribution of the background radiation under particular experimental conditions, among them non-evacuated beam paths [15]. While in a few cases X-ray spectrometers have been enclosed in vacuum chambers [16–18], most of the IXS and XES spectrometers are operated in air. For those experiments requiring a reduction of the intensity of background radiation to enhance the signal-to-background ratio, He-filled bags are usually introduced into the beam paths within the spectrometer.

It is the aim of this work to investigate the background owing to parasitic scattering originated by radiation scattered from the beam paths in Johann-type spectrometers. An analytical calculation formalism to simulate the energy distribution of the background radiation intensity in IXS and XES experiments is presented. Additional structures introduced into the IXS/XES measured spectra by the background radiation and, more generally, the validity of approximating the background by a constant or a lineal function will be discussed. The dependence of the background radiation on several experimental and geometrical parameters will be studied.

2. Calculation formalism

In this section, a general calculation formalism to compute the spectral distribution of background radiation in IXS and XES experiments is presented. It is considered that the experiments are performed using Johann-type spectrometers in Rowland geometry. The background radiation is assumed to be originated by scattering of X-ray photons in the non-evacuated beam paths of the spectrometer. A schematic of a Johann-type spectrometer is shown in Fig. 1. Briefly, the principle of operation is as follows. A spherically bent crystal analyser collects photons emitted from the sample into a solid angle $\Delta\Omega_A$, analyses a narrow energy window of the spectrum and then focuses the analysed radiation onto the detector. Sample, analyser and detector are located on the Rowland circle. In order to perform the calculations, some simplifying assumptions have been considered. The photon beam transmitted through the sample is absorbed by a beam stopper located close to the sample. Under this situation, only scattering events along the beam paths of photons emitted by the sample contribute to the measured background radiation. The sample is assumed to be punctual and the detector to have a finite area. The photons outgoing from the sample in directions other than those collected by the analyser are absorbed by a collimator placed in front of the sample (see Fig. 1(a)). Additionally, the solid angle collected by the analyser is assumed to be small. Under these assumptions, the divergent beam emitted by the sample, passing through the collimator and reaching the analyser can be replaced by a straight beam of the same intensity, scattered into an angle θ (central beam in Fig. 1(a)). The beam direction is the line joining the sample with the centre of the analyser crystal. Therefore, the dependence on the take-off angle θ, within the small solid angle collected by the analyser, can be disregarded. The present calculation formalism considers the contribution to the background radiation intensity due to elastic and inelastic scattering processes along the whole length of

the beam paths. For the sample-analyser beam path (beam path 1), all spectral components of the beam emitted by the sample are taken into account. Under the approximations assumed, the background radiation intensity originated by photons of energy ω, scattered in the beam path 1 can be calculated from

$$
\begin{aligned}
B_1(\omega_0) = & \int_0^\infty \frac{dI}{d\omega}(\omega_0, \omega) \int_0^{R\sin(\theta_A)} e^{-\mu(\omega)x_1} \frac{d\sigma_{el}}{d\Omega} e^{-\mu(\omega)l_1} \\
& \times \Delta\Omega_D(\varphi_1)W(\omega)dx_1 d\omega \\
& + \int_0^\infty \frac{dI}{d\omega}(\omega_0, \omega) \int_0^{R\sin(\theta_A)} e^{-\mu(\omega)x_1} \frac{d\sigma_{inel}}{d\Omega} e^{-\mu(\omega_c)l_1} \\
& \times \Delta\Omega_D(\varphi_1)W(\omega)dx_1 d\omega
\end{aligned}
\tag{1}
$$

Similarly, for the analyser–detector beam path (beam path 2) the contribution to the background radiation intensity originated by scattering of the analysed photon beam of energy ω_A can be evaluated from

$$
\begin{aligned}
B_2(\omega_0, \omega_A) = & I_T(\omega_0, \omega_A) \int_0^{R\sin(\theta_A)} \int_{\Delta\Omega_D} e^{-\mu(\omega_A)x_2} \frac{d\sigma_{el}}{d\Omega} e^{-\mu(\omega_A)l_2} d\Omega_D dx_2 \\
& + I_T(\omega_0, \omega_A) \int_0^{R\sin(\theta_A)} \int_{\Delta\Omega_D} e^{-\mu(\omega_A)x_2} \frac{d\sigma_{inel}}{d\Omega} e^{\mu(\omega_c)l_2} d\Omega_D dx_2
\end{aligned}
\tag{2}
$$

The spectral distribution of the radiation emitted by the sample into the analyser solid angle $\Delta\Omega_A$, $dI/d\omega$, can be approximated by

$$
\frac{dI}{d\omega}(\omega_0, \omega) = \int_{\Delta\Omega_A} \frac{d^2I}{d\omega d\Omega}(\omega_0, \omega, \theta')d\Omega(\theta') \approx \frac{d^2I}{d\omega d\Omega}(\omega_0, \omega, \theta)\Delta\Omega_A(\theta)
\tag{3}
$$

where $\frac{d^2I}{d\omega d\Omega}(\omega_0, \omega, \theta')$ is the spectral distribution of the radiation emitted by the sample per unit solid angle and energy interval, with energy ω, in the direction θ' relative to the incident beam of energy ω_0. In Eqs. (1) and (2), $R\sin(\theta_A)$ is the sample-analyser and also the analyser–detector distance for Rowland geometry, where R is the curvature radius of the crystal analyser (or the Rowland circle diameter). The analysing crystal is set to operate at a diffraction angle θ_A. μ is the attenuation coefficient, x_1 (x_2) and l_1 (l_2) are the scattering position on the beam path 1 (2) and the distance between this point and the detector, respectively. $\frac{d\sigma_{el}}{d\Omega}$ and $\frac{d\sigma_{inel}}{d\Omega}$ are the differential cross sections for elastic and inelastic scattering, respectively. $\omega_c = \omega/[1 + \frac{\omega}{mc^2}(1 - \cos(\varphi))]$ is the Compton energy for the scattering angle φ, mc^2 is the electron rest energy. $\Delta\Omega_D(\varphi_1)$ is the solid angle subtended by the detector at the scattering point x_1, which is assumed to be small. W is the energy acceptance window of the detector, i.e., the width of the energy window of the single channel analyser of the detection system.

In Eq. (2), $I_T(\omega_0, \omega_A)$ is the radiation intensity at the energy ω_A, associated to the diffraction angle θ_A, transmitted by the analyser, which can be estimated by [16]

$$
I_T(\omega_0, \omega_A) = T_A \frac{dI}{d\omega}(\omega_0, \omega_A)
\tag{4}
$$

where $T_A = R_i \frac{\omega_A}{\tan(\theta_A)}$ is the analyser transmittance [16] and R_i is the integrated reflectivity of the crystal.

Geometrical parameters, as the distances l_1 and l_2, the scattering angles φ_1 and φ_2 and the solid angle $\Delta\Omega_D(\varphi_1)$, can be expressed as a function of the scattering position x_1 or x_2:

$$
\varphi_1 = 2\theta_A - \beta
\tag{5a}
$$

$$
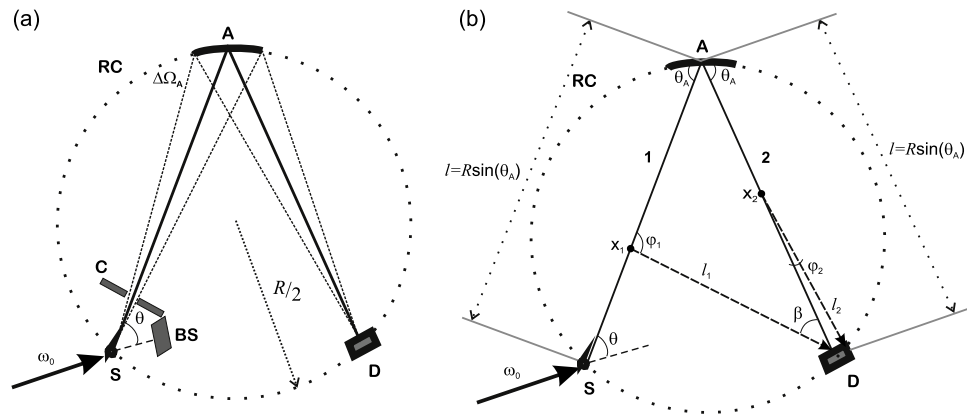\cos(\beta) = \frac{l_1^2 + 2x_1 l - x_1^2}{2ll_1}
\tag{5b}
$$

$$
l_1 = \sqrt{(l - x_1)^2 + l^2 + 2(l - x_1)l_1\cos(2\theta_A)}
\tag{5c}
$$

$$
l = R\sin(\theta_A)
\tag{5d}
$$

$$
\varphi_2 = \arctan\left(\frac{r}{l_2}\right)
\tag{5e}
$$

$$
l_2 = \sqrt{r^2 + (l - x_2)^2}
\tag{5f}
$$

$$
\Delta\Omega_D(\varphi_1) = A_D \frac{\cos(\beta)}{l_1^2}
\tag{5g}
$$

Fig. 1. (a) Scheme of a Johann-type spectrometer for inelastic X-ray scattering or X-ray emission spectroscopy. ω_0: incident beam energy, **S**: Sample, θ: sample scattering angle, **RC**: Rowland circle, **A**: Spherically bent analyser crystal of curvature radius R, **D**: Detector, **C**: Collimator, **BS**: Beam stopper. (b) Schematics of the contributions to the background radiation due to scattering of X-rays in the beam paths **1** (sample-analyser) and **2** (analyser–detector). θ_A: diffraction angle of the analyser. φ_1 and φ_2 are the scattering angles of the X-rays scattered into the detector in the beam path 1 or 2, respectively, while l_1 (l_2) is the distance between the scattering point x_1 (x_2) and the detector.

where A_D is the detector active area and r is the radial distance from the centre to the impinging point on the detector window.

By analysing the factors of the integrands in Eqs. (1) and (2), some general behaviours can be drawn. In Fig. 2, the dependence of $\Delta\Omega_D(\varphi_1)$ on the scattering point x_1 along the beam path is shown for different curvature radius and analyser diffraction angles. $\Delta\Omega_D(\varphi_1)$ has a sharp maximum very close to the sample position and decreases rapidly for larger distances. The maximum position shifts to smaller distances as the diffraction angle approaches $\frac{\pi}{2}$ (see Fig. 2(b)). Other factors in the integrand of Eq. (1) (as attenuation factors and cross sections) are monotonically varying functions of the position x_1. This indicates that the major contribution to the background radiation intensity arises from the beam path region in the close vicinity of the sample. In relation to the second beam path, since forward elastic scattering processes are mainly contributing, the intensity distribution $B_2(\omega_0, \omega_A)$ should resemble that of IXS or XES spectrum.

By using theoretical models or measured spectra as input for the spectral distribution of radiation emitted by the sample in Eqs. (1) and (2), the intensity of the background radiation can be calculated for different experimental conditions. Although in the present study the calculations will be made for specific samples, the discussion of the results will have general validity and can be applied to other IXS or XES experiments.

To perform the numerical evaluation of Eqs. (1) and (2), values of the absorption coefficients from the XCOM database [19] were used and values of the incoherent scattering function and of the atomic form factor were taken from the tabulations of Ref. [20]. The discrepancy between theoretical and experimentally determined cross sections was found to be of the order of 10%–15% for low Z elements and for momentum transfers of the order of those involved in the experimental situation studied in this work [21]. Thus, it is expected that the accuracy of present background calculations would be of that order. The integrated reflectivity of the crystal analysers was evaluated with the XOP program [22]. A detector with an effective detection area of 25 mm^2 was assumed. If the spot of the beam focused by the analyser is much smaller than the detector entrance window, a diaphragm may be placed in front of the detector. In this case, the detector area must be replaced by the diaphragm area in Eq. (5g). The intrinsic detection efficiency was considered to be constant over all the accepted energy range.

3. Background radiation in IXS experiments

3.1. General considerations and calculation details

In IXS experiments performed in inverse geometry, which is the usual mode for energy analysis close to the backdiffraction condition, the
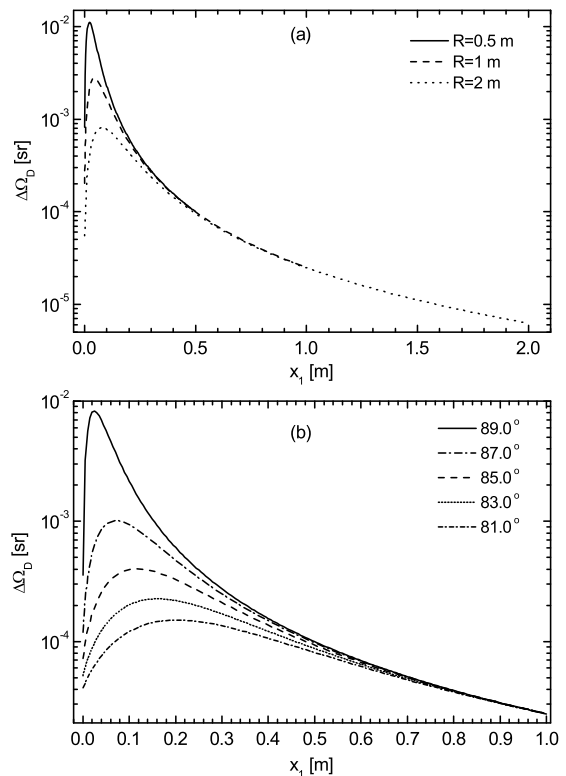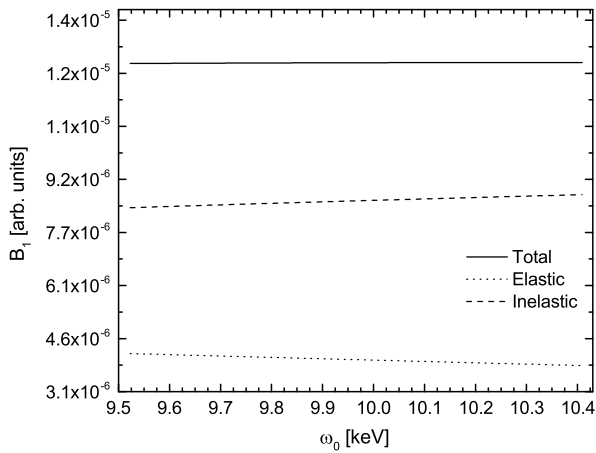

Fig. 2. (a) Solid angle subtended by the detector $\Delta\Omega_D$ as a function of the scattering point x_1 along the first beam path for three typical values of analyser curvature radius and for a fixed diffraction angle $\theta_A = 88.23°$. An effective detection area of 25 mm^2 was assumed. (b) As (a) but for different analyser diffraction angles and for a curvature radius $R = 1$ m.

energy-loss spectrum is measured by varying the incident photon energy ω_0 while keeping the analysed energy ω_A fixed. Hence, sample, analyser and detector are kept fixed on the Rowland circle of the spectrometer. The energy transfer ranges typically from a few tens of eV to several hundreds of eV. Eq. (1) requires, as input quantity, the IXS spectrum of the scattering sample as a function of ω_0 and for a given momentum transfer. This spectral distribution is proportional to the double differential scattering cross section (DDCS) of the scattering electron system. DDCS for collective and individual electron excitations can be described
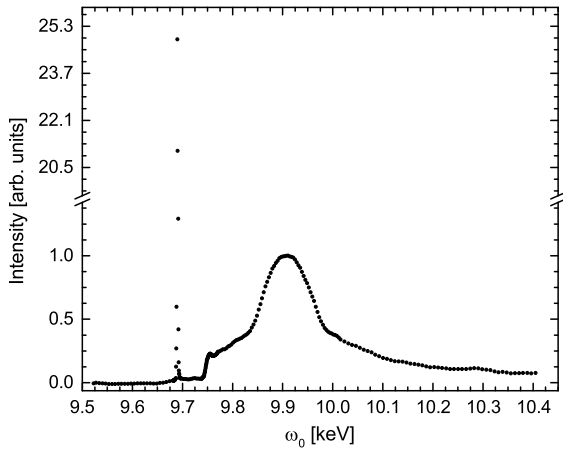
Fig. 3. IXS spectrum of Li metal measured for a momentum transfer of 4.3 a.u. The elastic line, the onset of the 1s electron excitation spectrum at ~55 eV energy transfer and the valence electron excitation spectrum exhibiting a maximum at ~220 eV energy transfer can be distinguished. The data processing is indicated in the text. The amplitude of the main IXS peak was normalised to the unity.

Fig. 6. Background radiation intensity in an IXS experiment originated in the sample-analyser beam path as a function of the incident photon energy for different analyser curvature radii R. Note that for each value of curvature radius a different intensity scale has been used. Other calculation details as in Fig. 4.
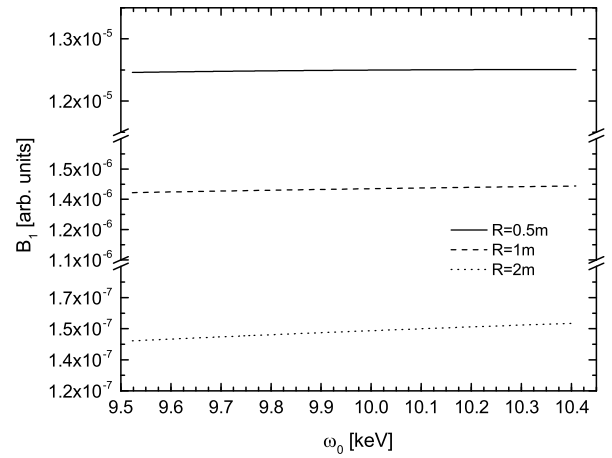

Fig. 4. Background radiation intensity originated in the sample-analyser beam path (solid line) as a function of the incident photon energy for an IXS experiment. The contributions from elastic (dotted line) and inelastic (dashed line) events to the background radiation are shown separately. The calculations were made for beam paths in air and for a spherically bent Si 660 crystal analyser of 0.5 m curvature radius. The analysed energy was 9.69 keV.
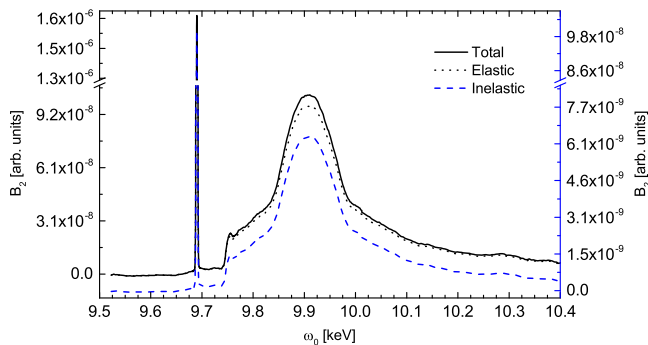
Fig. 5. The same as Fig. 4 but for the analyser–detector beam path. The right axis corresponds to the inelastic scattering contribution.

using simple theoretical models for the dielectric response function as that from Lindhard [23]. Sophisticated first-principle models based

on time-dependent density functional theory or many particle Green's functions [24] are used to describe the energy-loss function by valence electron excitation in different systems [25–27]. To model inelastic X-ray scattering from core electrons, theoretical algorithms based on the multiple scattering formalism [28,29] as well as methods based on the Bethe–Salpeter equation [30,31] have been developed. Nevertheless, if available, experimental electron-excitation spectra would provide a more realistic description for the spectral distribution of radiation scattered by the sample.

The calculation formalism is illustrated for the case of an IXS spectrum of Li metal at $q = 4.0$ a.u. momentum transfer. In the present work, the spectral distribution $\frac{dI}{d\omega}$ is built from a measured IXS spectrum according to:

$$I = \frac{dI}{d\omega}(\omega_0, \omega_A) \exp(-\mu l_1) T_A \exp(-\mu l_2) \ , \tag{6}$$

where energy dependent corrections arising from beam attenuation in both spectrometer beam paths and analyser transmittance were applied. The Li IXS spectrum was measured at the XDS beamline of the Laboratório Nacional de Luz Síncrotron (LNLS) using a Johann-type spectrometer in Rowland geometry. A Si 660 spherically bent crystal analyser of curvature radius $R = 0.5$ m and operated at a diffraction angle $\theta_A = 88.23°$ was used. The corresponding analysed energy was $\omega_A = 9.69$ keV and the incident photon energy ranged from 9.5 keV to 10.4 keV. The scattering angle was set to $\theta = 100°$. The overall energy resolution was determined from the width of the elastic peak to be 1.5 eV. The measured spectrum was normalised to the monitor detector signal to correct for intensity fluctuations in the incident beam and for the slow decay of the electron beam current of the ring. A constant background was subtracted from the experimental data. The obtained spectral distribution $dI/d\omega$ is displayed in Fig. 3.

The energy acceptance window of the detector in Eqs. (1) and (2) was considered to be open to collect the whole scattered spectrum. Since IXS experiments are usually performed on samples of low atomic number, the low energy fluorescence radiation emitted by the sample will not contribute to the background radiation registered by the detector.

3.2. Results

The background radiation intensities originated in the sample-analyser and analyser–detector beam paths in an IXS experiment are shown in Figs. 4 and 5, respectively. Air paths in the spectrometer were assumed. The energy analysis was considered to be made by using
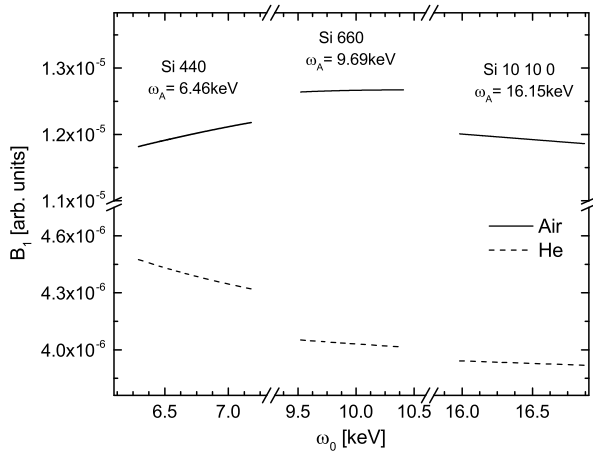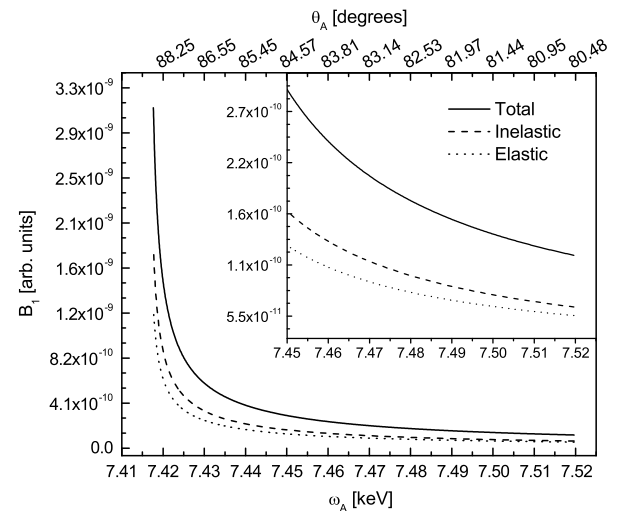
Fig. 7. Background radiation intensity in an IXS experiment originated in the sample-analyser beam path for two different media: air (solid line) and helium (dashed line). The dependence on the analysed energy, corresponding to different Si $hh0$ reflections, is also shown. Other calculation details as in Fig. 4. Note the different intensity scales used for air and helium.

Fig. 8. Background radiation intensity originated in the sample-analyser beam path (solid line) as a function of the analysed energy for an XES experiment. Diffraction angles, corresponding to the analysed energies, are shown on the top axis. Elastic (dotted line) and inelastic (dashed line) contributions are shown separately. The calculations were made for beam paths in air and for a spherically bent α–quartz $4\bar{4}04$ crystal analyser of 1 m curvature radius. The inset show the high energy tail in more detail.

a Si 660 spherically bent crystal analyser with a curvature radius of 0.5 m and set to analyse 9.69 keV X-ray photons. The inelastic scattering component in the sample-analyser beam path is larger by a factor ~2 and shows a slight linear increase, while the elastic component diminishes slightly in the same energy range. The scattering angle φ_1 for a photon scattered into the detector direction (see Fig. 1) varies along the first beam path from $\varphi_1 = \theta_A$, for scattering processes occurring close the sample, to $\varphi_1 = 2\theta_A$, for scattering processes close to the analyser. Since θ_A is usually near $\pi/2$ and ω_A is of the order of several keV, the differential cross section for inelastic scattering is larger than that for elastic scattering in all the range of scattering angles allowed by the geometry of the spectrometer and in the range of energies of the present studies. Additionally, the energy dependence of the scattering cross sections dominates over the attenuation factor in Eq. (1) within the energy range covered in the experiment. This accounts for the observed energy dependence and for the intensity ratio between both partial components. The total intensity of the background radiation is nearly constant within the studied energy range.
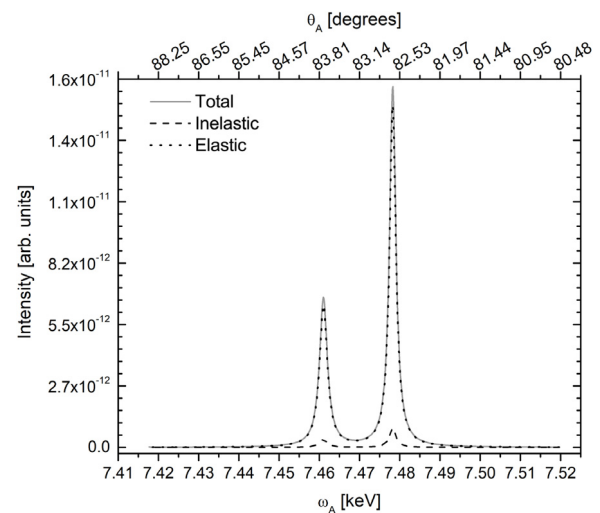
Since the energy integration range in Eq. (1) is limited by $W(\omega)$ and in typical IXS experiments $W(\omega)$ is set to several hundreds of eV, characteristic spectral structures of the IXS spectrum are not reproduced in the background radiation, as Fig. 4 shows. For the hypothetical case of an energy acceptance window as narrow as the experimental energy resolution (usually of the order of 1 eV), the spectral distribution of the background radiation would be proportional to $\frac{dI}{d\omega}$, and thus resembling all its spectral features, as can be easily shown by setting $W(\omega) \sim \delta(\omega - \omega_A)$ in Eq. (1).

For the second spectrometer beam path, the analyser–detector beam path, the energy distribution of the background radiation resembles that of the spectral distribution of the radiation scattered by the sample (see Fig. 5). Unlike the first beam path, the dominant contribution arises from elastic scattering processes. It is known that the atomic differential cross section for inelastic scattering vanishes for scattering angles going to zero, while the differential cross section for elastic scattering peaks at forward scattering. Since most of the scattered radiation along this beam path, entering the detector, is scattered into small angles, elastic scattering processes provide the major contribution to the background radiation in the second beam path, as Fig. 5 shows.

The comparison between Figs. 4 and 5 shows that the background radiation intensity is originated mostly in the first beam path. At characteristic energies of the IXS spectrum (around the maximum of the valence part), the contribution from B_1 is at least two order of magnitude


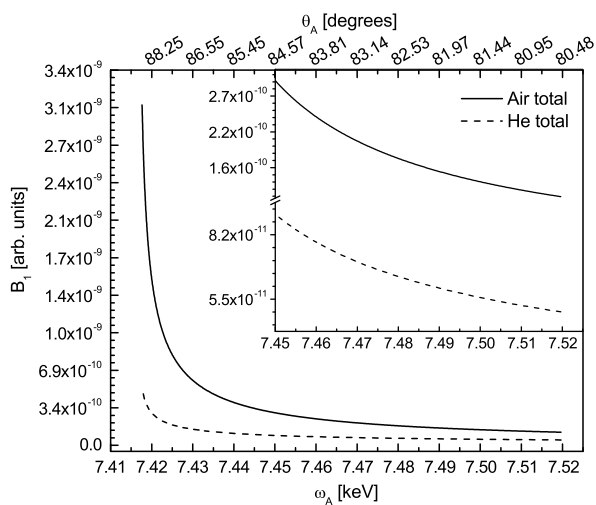**Fig. 9.** The same as Fig. 8 but for the analyser–detector beam path.

more intense than that from B_2. This high is mainly a consequence of the small transmittance of the Si crystal analyser.

By estimating the signal intensity of the IXS spectrum with Eq. (6), the signal-to-background ratio at the maximum of the valence IXS spectrum can be evaluated to ~38. In addition, since the relative contribution of the analyser–detector beam path to the total background intensity at that energy is ~10^{-2}, the structures introduced by the background radiation in the detected IXS spectrum should not be appreciable.

Since the first beam path provides the main contribution, from now on, only B_1 will be taken into account to study the influence of several experimental configurations on the background radiation. The effect of the size of the Rowland circle on the intensity of the background radiation is displayed in Fig. 6. As a function of the energy, the trends are very similar, showing a slight linear increase, somewhat more pronounced for the largest analyser curvature radius (about 7% in the investigated energy range). For typical curvature radii, the magnitude of background radiation diminishes by about one order of magnitude as
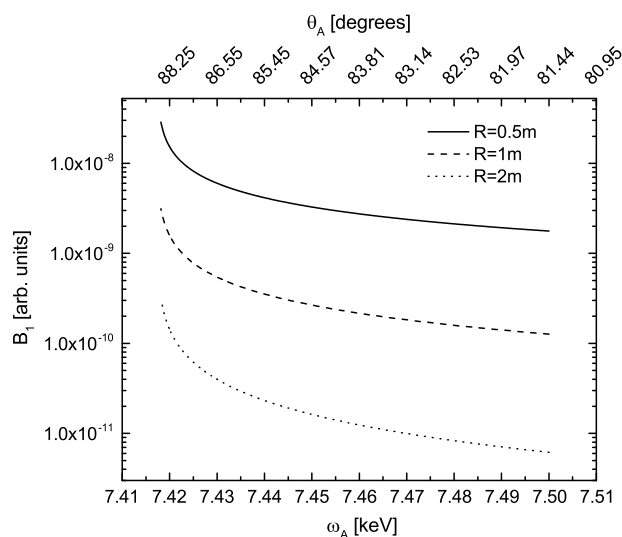
Fig. 10. Background radiation intensity in an XES experiment originated in the sample-analyser beam path for different analyser curvature radii R. Diffraction angles, corresponding to the analysed energies, are shown on the top axis. Other calculations details as in Fig. 8.

Fig. 12. Background radiation intensity in an XES experiment originated in the sample-analyser beam path for different α-quartz crystal analyser reflections. The analysed energy ranges corresponding to $4\bar{4}04$ (Ni $K\alpha_{1,2}$), $6\bar{6}06$ (Se $K\alpha_{1,2}$) and $8\bar{8}08$ (Y $K\alpha_{1,2}$) reflections were 7.42 keV$\leq \omega_A \leq$ 7.52 keV, 11.13 keV$\leq \omega_A \leq$ 11.25 keV and 14.84 keV$\leq \omega_A \leq$ 15.00 keV, respectively. A curvature radius of 1 m was assumed.
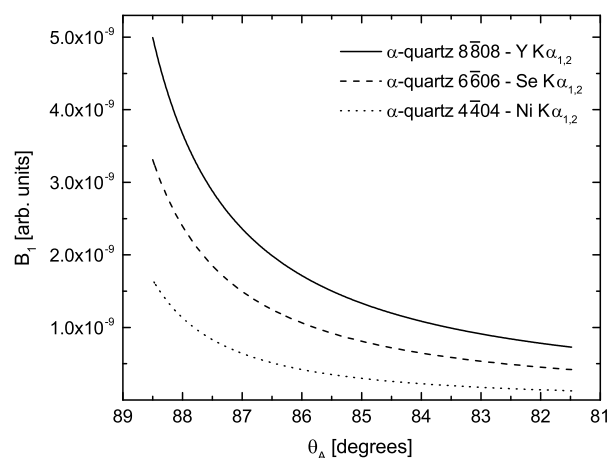

Fig. 11. Background radiation intensity in an XES experiment originated in the sample-analyser beam path for two different media: air (solid line) and helium (dashed line). Diffraction angles, corresponding to the analysed energies, are shown on the top axis. Other calculations details as in Fig. 8.

the size of the Rowland circle is doubled, as shown by Fig. 6. In part, this behaviour is ascribed to geometrical effects, particularly to the dominant effect of the detector solid angle, as previously discussed. Radiation attenuation effects between the scattering point and the detector also contributes to the diminishing intensity of background radiation with increasing Rowland circle radius.

The influence of the type of gas filling the beam paths on the intensity of background radiation is illustrated in Fig. 7. Calculations were performed for dry air and for He-filled beam paths. In the same figure, the dependence on the analysed energy is also shown. Analysed energies of 6.46 keV, 9.69 keV and 16.15 keV were considered. These energies correspond to the 440, 660 and 10 10 0 reflections of a Si analyser crystal operated at a fixed diffraction angle of 88.23°, respectively.

As expected, because of the larger mean atomic number of air, the background radiation generated in beam path in air is much stronger than that for a helium-filled beam path. As a function of the analysed

energy, the average background radiation intensity increases from lower to middle energies and decreases at higher energies for a beam path in air. Unlike, for a helium-filled beam path, a monotonous decrease can be observed as the analysed energy increases. The general trend observed for the case of air can be traced back mainly to the relationship between attenuation effects and the effective interaction volume for different energies. As can be seen from Fig. 2, the effective interaction region is limited to the first few cm of the beam path. This is a pure geometrical effect, which is independent of the analysed energy. At lower energies, attenuation effects of the scattered photons between the interaction point and the detector are more significant. On the other hand, at higher energies the interaction probability within the effective interaction volume is relatively smaller. Consequently, the intensity of the background radiation should reach a maximum around middle energies, in consistency with the calculations. This trend is not observed for helium-filled beam paths because the investigated energies are not low enough. Concerning the dependence on the incident photon energy, Fig. 7 shows an almost linear dependence at medium and high analysed energies, while at lower energies a slight departure from the linearity was found, in particular for a helium-filled beam path. Because of stronger attenuation effects, a rapid variation of the background radiation intensity within the interval of scanned incident energies is expected at low analysed energies.

The present results show that in IXS experiments performed in usual conditions, the subtraction of a linear background from the measured spectrum should be adequate in most cases. The determination of the linear background can be accomplished by fitting a linear function in a sufficiently wide energy interval on the low energy side of the elastic line. The fitted function can then be extrapolated to the whole measured energy range and subtracted from the recorded spectrum.

4. Background radiation in XES experiments

4.1. General considerations and calculation details

In XES experiments, the X-ray spectrometer of Fig. 1 is operated in scanning mode. The analysis of the X-ray emission spectrum in a narrow energy interval, usually several tens of eV, is performed by scanning the analyser in synchrony with the detector. The excitation energy ω_0 of the incident X-ray beam is kept fixed.
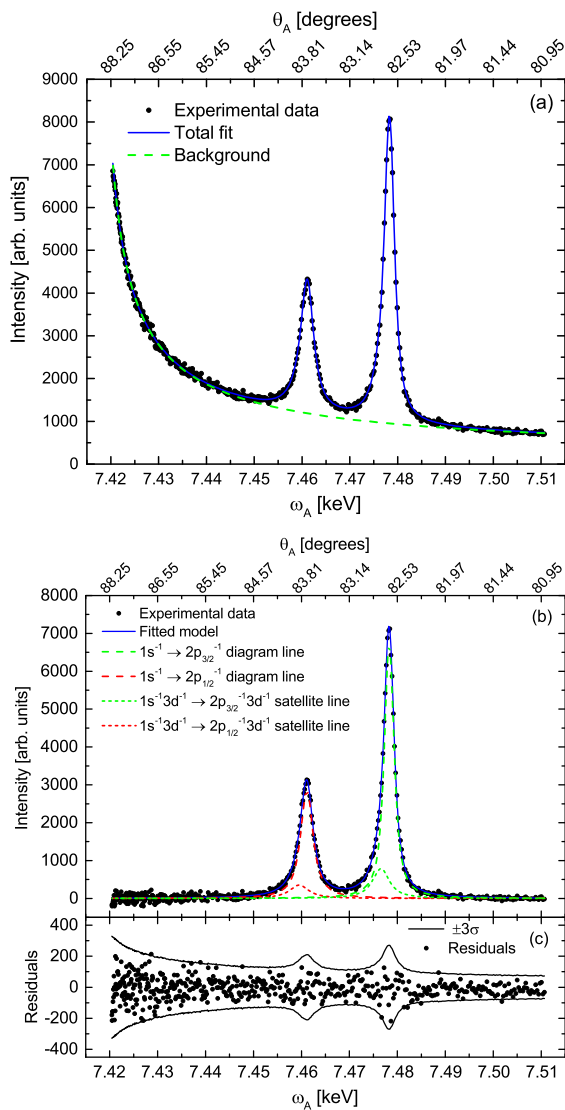
Fig. 13. (a) Experimental Ni $K\alpha_{1,2}$ emission spectrum (symbols). The total fit (see text) (solid line) and the fitted background (dashed line) are shown separately. Diffraction angles, corresponding to the analysed energies, are shown on the top axis. (b) Background-subtracted emission spectrum. The individual fitting components are also shown. (c) Fitting residuals. Also shown are the limits of the $\pm 3\sigma$ band, σ being the statistical uncertainty.

The X-ray emission spectrum $\frac{dI}{d\omega}$ in Eqs. (1) and (2) can be described by a simple analytical model, which consists of a sum of Lorentzian functions [32] representing diagram and potential satellite lines due to shake processes. In the case of the $K\beta_{1,3}$ spectra of transitions metals, the characteristic distorted line shape can be also simulated by a sum of Lorentzian functions in order to take into account the asymmetry introduced by atomic multiplets [32,33]. Depending on the excitation energy, satellite lines due to spectator hole transitions may be present in the XES spectrum. Usually, these satellite lines give rise to an asymmetry and can be as strong as about 40% of the intensity of the diagram lines, as it is the case of 3d spectator hole transitions in Fe [34]. Another deexcitation channel, which may contribute to the distortion of the line shape, is the radiative Auger effect (RAE). Although KLL and KMM RAE transitions are weak in relation to the $K\alpha$ line intensity [35,36], RAE satellites accompanying valence-to-core electronic transitions can appreciably distort the $K\beta_{2,5}$ line shape [37]. RAE line shapes can be described by an analytical model as that proposed in Ref. [37].

The calculation model for the background radiation in XES experiments is illustrated for the case of the $K\alpha_{1,2}$ emission spectrum of Ni. The spectral distribution of the Ni $K\alpha_{1,2}$ spectrum, $\frac{dI}{d\omega}$ in Eq. (3), was modelled using Lorentzian functions, which describe the diagram lines corresponding to the $2p^{-1} \rightarrow 1s^{-1}$ transitions [15]. The spectral parameters (line widths and relative intensities) were taken from Ref. [15]. The energy of the $K\alpha_1$ was set to the reference value from Ref. [38]. The energy analysis was assumed to be performed with an α–quartz spherically bent crystal analyser using the $4\bar{4}04$ reflection. This analyser was demonstrated to be well suited to measure the Ni $K\alpha$ spectrum in near backdiffraction condition [15]. The spectral distribution $\frac{dI}{d\omega}$ was normalised such that the $K\alpha_1$ emission line peaks to unity.

It is further assumed that only the $K\alpha_{1,2}$ emission spectrum was detected. This is achieved by closing the width of the acceptance energy window of the detector to 1.0 keV around the $K\alpha_1$ line energy. This energy window is wide enough to accept photons form the whole $K\alpha_{1,2}$ spectrum, while rejecting contributions from the $K\beta$ spectrum.

4.2. Results

The background radiation for the sample-analyser and analyser–detector beam paths in air are displayed in Figs. 8 and 9, respectively. An analyser curvature radius of 1 m was assumed. As observed and discussed for IXS measurements, inelastic scattering processes are the main contribution to the total background intensity originated in the first beam path. Unlike IXS experiments, a steep rise in the intensity of the background radiation in XES experiments is noticeable on the low energy side (diffraction angles close to $\pi/2$) for both contributions in the first beam path. The origin of this behaviour is geometrical, more specifically, it is a consequence of the rapid increase of the detector solid angle as the analyser diffraction angle approaches $\pi/2$ (see Fig. 2(b)). It is worth noting that this effect is an intrinsic characteristic of the Rowland geometry of Johann-type spectrometers. On the high energy side, the intensity of the background radiation diminishes slowly. A second order polynomial has proven to be appropriate to describe the experimental background radiation in this energy region [15]. In relation to the analyser–detector beam path (see Fig. 9), the energy distribution of the background radiation resembles the spectrum emitted by the sample and the elastic scattering processes provide the major contribution, in a similar way to the case of IXS experiments.

The comparison of Figs. 8 and 9 shows that the major contribution to the total background radiation intensity is provided by the sample-analyser beam path. The contribution from the analyser–detector beam path at the energies of the $K\alpha_{1,2}$ lines, where its spectral distribution peaks, is about one order of magnitude less than that from the first beam path. As previously discussed, this result is assigned to the narrow transmission of the analyser crystal. However, the ratio between the contributions from each beam path is smaller than that for the case of IXS experiments. This is a consequence of the high integrated reflectivity of an α–quartz crystal in comparison to a Si crystal for the considered reflections.

From the estimation of the signal intensity of the XES spectrum by using Eq. (6), the ratio between the area of the diagram lines and that from the spurious peaks introduced by the background radiation originated in the analyser–detector beam path can be estimated to $\sim 2 \times 10^{-4}$. Hence, measured intensities of the diagram lines should not be altered by the peak structures introduced by the background radiation appreciably.

In relation to the dependence of the background radiation on the size of the Rowland circle, Fig. 10 shows an increase of intensity as the Rowland circle diameter diminishes. As already discussed for the case of IXS measurements, this trend has mainly a geometrical origin.

To investigate the effect of the type of gas filling the beam paths on the background radiation, calculations were performed for a helium-filled beam path and for a beam path in air. The results are shown in Fig. 11. Owing to the lower density and lower atomic number of He, the

generated background radiation in a He-filled beam path is less intense than for the case of air. Fig. 11 shows that by replacing an air-by a helium-filled beam path, the intensity of background radiation can be diminished by a factor ranging from ~6 to ~2 in the investigated energy range and for a 1 m diameter Rowland circle. It should be noticed that due to weaker absorption effects, the signal-to-background ratio should be enhanced by a factor even higher for the case of helium-filled beam paths.

The intensity of background radiation for XES experiments performed at different crystal analyser reflections is shown in Fig. 12 for the spectrometer first beam path. In the case shown, the $6\bar{6}06$ and $8\bar{8}08$ reflections of an α–quartz crystal are assumed to be used to analyse the $K\alpha_{1,2}$ emission spectra from Se and Y, respectively. The $K\alpha_1$ and $K\alpha_2$ emission lines were modelled by Lorentzians located at the energies given by Ref. [38]. Line-widths from Ref. [39] and the line fraction calculated by Scofield [40,41] were used. The results show a similar energy dependence within the analysed energy ranges, with an overall increase in the background radiation intensity for larger reflection orders. The ratio between Se (Y) and Ni background radiation intensities ranges from ~3 (~5), for low Bragg diffraction angles, to ~2 (~3) for analysed angles close to the backdiffraction condition. As mentioned previously for the case of IXS, the magnitude of the background radiation intensity is determined by the interplay between attenuation effects, the inelastic scattering cross section and the effective interaction volume. A decrease in the intensity of the background radiation for XES experiments can be expected for much higher analysed energy ranges than those typically used in IXS.

The need for an accurate background correction in high resolution XES experiments is evidenced by Figs. 8 and 10–12. Particular attention must be paid to those measurements of X-ray emission lines made at analyser diffraction angles very close to $\pi/2$, where the variation of the background radiation intensity with the diffraction angle/energy is very rapid. More critical are those experiments performed with beam paths in air and using spectrometers of small Rowland circle radius. Under this situation, the background correction procedure requires simulating its spectral distribution, properly scaling to the measured intensity, for instance by a fitting procedure, and, finally, subtracting from the measured spectrum. At smaller analyser diffraction angles, the energy dependence is smoother and a second order polynomial could be adequate to simulate the background radiation [15]. Some atomic excitation processes accompanying inner-shell vacancy creation, as for instance 3s and 3p shake processes as the result of 1s vacancy production in transition metals, have been predicted to be of very small probability [42]. Precise studies of such shake transitions by means of high resolution X-ray emission spectroscopy might demand an accurate description of the background radiation to correctly assess the associated satellite lines in the measured spectra.

As a test case for proving the accuracy of the model in a realistic experimental situation, the simulated background radiation was introduced in a subtraction procedure with the aim to extract the XES spectrum from the row measured data. An XES spectrum was measured under experimental conditions that should enhanced the effects of background radiation on the measured spectrum (see Fig. 13(a)). A Johann-type spectrometer with a Rowland circle of 1 m diameter and with beam paths in air was used to measure the Ni $K\alpha_{1,2}$ spectrum. The energy analysis was accomplished with a $4\bar{4}04\alpha$–quartz spherically bent crystal, which allows the Ni $K\alpha_{1,2}$ lines to be analysed close to the backdiffraction condition. The achieved energy resolution was 1.07 eV at the energy of the $K\alpha_1$ line. The energy of the incident X-ray beam was set to 8.4 keV, hence spectator hole satellites other than $1s^{-1}3d^{-1}$ are not excited [15]. The measurements were performed at the XDS beamline of the Brazilian Synchrotron Light Laboratory (LNLS). Further experimental details are given elsewhere [15].

A fitting procedure as the one used in Ref. [15] was implemented. As proposed in Ref. [15], the spectral components, including both diagram and satellite lines, were modelled by Lorentzian profiles, which

were convolved by a Gaussian response function to take into account instrumental resolution effects. This model for the XES spectrum, superimposed on the calculated background, was fitted to the experimental data. The fitting was performed by using least-squares regression, which minimises the weighted sum of residuals. The inverse of the squared experimental uncertainty was taken as weight. In addition to the parameters defining position, amplitude and width of the Lorentzian profiles, a scaling factor of the calculated background and a constant were taken as fitting parameters. That constant needs to be included to describe a constant background contribution of stray radiation that is originated by scattering from different parts of the spectrometer and that cannot be accounted for by analytical models.

The background-subtracted spectrum after fitting along with the individual fitting components of the XES spectrum and the fitting residuals are displayed in Fig. 13(b) and (c), respectively. Though the measured spectrum is superimposed on a strong, non-linear background radiation, the main diagram lines, corresponding to the $K\alpha_{1,2}$ emission lines, and two low-energy satellites could be clearly resolved by the fitting procedure. These satellite lines have been identified in a previous work [15] as originated by $2p \rightarrow 1s$ electronic transitions with a 3d spectator hole created by shake processes. The fitting results yield a separation between the diagram lines of 17.2 eV, which is in very good agreement with the value obtained from more refined measurements of the Ni $K\alpha_{1,2}$ spectrum [15] and with the measurements from Hölzer et al. [32]. The obtained $K\alpha_2$–to–$K\alpha_1$ intensity ratio for the pure diagram lines of 55% is also in good agreement with previous experiments. Concerning shake satellites, two peaks located 1.7 eV and 1.6 eV towards lower energies from the main diagram lines and having intensity ratios of 21% and 19%, relative to the $K\alpha_1$ and $K\alpha_2$ lines respectively, were found. These spectral parameters are very close to previously measured values [15]. Present values for the satellite intensity ratios provide a further validation of calculations based on multi-configuration atomic models [10], which predicted a total shake probability of about 22%.

The residuals, which are randomly distributed within the $\pm 3\sigma$ error band, show no systematic bias in the whole energy range. This indicates the present model is able to describe with high accuracy the spectral distribution of the background radiation, at least within the limits of the experimental uncertainties.

In those regions where contributions from the X-ray emission lines are not expected (low and high energy regions of the spectrum), the measured intensity is well described by the background radiation model. Particularly, a very good fitting can be observed in the low energy region, where the intensity originated from scattering along the sample-analyser beam path increases rapidly as the analyser diffraction angle approaches to $\pi/2$.

5. Conclusions

A calculation formalism to evaluate the background radiation in IXS and XES experiments performed with Johann-type spectrometers was presented. The calculation model takes into account the background radiation originated by scattering processes along the beam paths in the spectrometer. Different conditions realised in usual experiments were investigated. In IXS as well as in XES experiments, the background radiation is mainly originated in the sample-analyser beam path. In this beam path, the contribution from inelastic scattering events dominates over that from elastic ones, though the order of magnitude are comparable. The calculations show that most of the scattered radiation arises from scattering interactions occurring in a beam path region very close to the sample. This result indicates that the signal-to-background ratio can be enhanced by properly shielding the detector from the background radiation arisen from the first part of the beam path.

For IXS measurements, the spectral distribution of the background radiation originated from single scattering events can be well described by a constant or a linear function for realistic experimental situations. This trend was found to be independent of the Rowland circle diameter.

In general, the subtraction of a linear background, as determined from the low energy side of the elastic line in the energy-loss spectrum, should be adequate. A possible exception would be those experiments performed with He-filled beam paths and for low analysed energies, where a slight departure from a linear background could be expected. For XES experiments, the calculation formalism predicts a rapid increase of the background radiation intensity for analyser diffraction angles approaching the exact backdiffraction condition. At lower angles, the background radiation could be described by a slow varying function.

The spectral distribution of background radiation originated in the analyser–detector beam path exhibits strong structure and resembles the measured spectrum, both for IXS and XES experiments. Nevertheless, owing to its negligible contribution in comparison to that from the sample-detector beam path, those characteristic structures should not distort the measured signal appreciably. In the case of IXS experiments the background radiation should not introduce additional structures into the measured energy-loss spectra. In relation to XES experiments, the spurious peaks introduced by the background radiation should not affect the determination of relative intensities of shake satellites to a large extent.

The calculation model was tested for a real experimental situation related to a measurement of the Ni $K\alpha$ emission spectrum with an underlying strong and non-linear background radiation. The calculated background radiation, along with a model for the XES spectrum, were introduced in a fitting procedure. The background-subtracted XES spectrum is in very good accordance, both concerning spectral shape and parameters, with previous measurements performed under much better experimental conditions in relation to signal-to-background ratio. The proposed calculation model was able to reproduce the spectral distribution of the experimental background radiation adequately, in particular at high analyser diffraction angles. The considered test case demonstrates the need of calculating background profiles to be used in background subtraction procedures for some experimental situations.

Acknowledgements

References

[1] W. Schülke, Electron Dynamics by Inelastic X-Ray Scattering, OUP, Oxford, 2007.

[2] J.-P. Rueff, A. Shukla, Inelastic X-ray scattering by electronic excitations under high pressure, Rev. Modern Phys. 82 (2010) 847–896. http://dx.doi.org/10.1103/RevModPhys.82.847.

[3] S.K. Lee, P.J. Eng, H.-k. Mao, Probing of pressure-induced bonding transitions in crystalline and amorphous earth materials: Insights from X-ray Raman scattering at high pressure, Rev. Mineral. Geochem. 78 (1) (2014) 139–174. http://dx.doi.org/10.2138/rmg.2014.78.4. arXiv:http://rimg.geoscienceworld.org/content/78/1/139.full.pdf. http://rimg.geoscienceworld.org/content/78/1/139.

[4] G.E. Stutz, M. Otero, S.A. Ceppi, C.B. Robledo, G. Luque, E. Leiva, D.E.B. Daz, Intercalation stage dependence of core electronic excitations in Li-intercalated graphite from inelastic X-ray scattering, Appl. Phys. Lett. 110 (25) (2017) 253901. http://dx.doi.org/10.1063/1.4986922.

[5] E. Gallo, P. Glatzel, Valence to core X-ray emission spectroscopy, Adv. Mater. 26 (46) (2014) 7730–7746. http://dx.doi.org/10.1103/PhysRevA.67.022510.

[6] P. Glatzel, U. Bergmann, High resolution $1s$ core hole X-ray spectroscopy in $3d$ transition metal complexes-electronic and structural information, Coord. Chem. Rev. 249 (1) (2005) 65–95. http://dx.doi.org/10.1016/j.ccr.2004.04.011.

[7] S. Limandri, S. Ceppi, G. Tirao, G. Stutz, C. Snchez, J. Riveros, High resolution study of K and K1,3 X-ray emission lines from Mn-compounds, Chem. Phys. 367 (2) (2010) 93–98. http://dx.doi.org/10.1016/j.chemphys.2009.11.001. http://www.sciencedirect.com/science/article/pii/S0301010409003383.

[8] T.L. Pham, T.V. Nguyen, J.A. Lowe, I.P. Grant, C.T. Chantler, Characterization of the copper Kβ x-ray emission profile: an *ab initio* multi-configuration Dirac-Hartree-Fock approach with Bayesian constraints, J. Phys. B: At. Mol. Opt. Phys. 49 (3) (2016) 035601. http://dx.doi.org/10.1088/0953-4075/49/3/035601.

[9] C.T. Chantler, J.A. Lowe, I.P. Grant, High-accuracy reconstruction of titanium x-ray emission spectra, including relative intensities, asymmetry and satellites, and ab initio determination of shake magnitudes for transition metals, J. Phys. B: At. Mol. Opt. Phys. 46 (1) (2013) 015002. http://dx.doi.org/10.1088/0953-4075/46/1/015002.

[10] J.A. Lowe, C.T. Chantler, I.P. Grant, Ab initio determination of satellite intensities in transition-metal photoemission spectroscopy using a multiconfiguration framework, Phys. Rev. A 83 (2011) 060501. http://dx.doi.org/10.1103/PhysRevA.83.060501.

[11] H. Sternemann, C. Sternemann, G.T. Seidler, T.T. Fister, A. Sakko, M. Tolan, An extraction algorithm for core-level excitations in non-resonant inelastic X-ray scattering spectra, J. Synchrotron Radiat. 15 (2008) 162. http://dx.doi.org/10.1107/S0909049508001696.

[12] S. Huotari, T. Pylkkänen, J.A. Soininen, J.J. Kas, K. Hämäläinen, G. Monaco, X-ray-Raman-scattering-based EXAFS beyond the dipole limit, J. Synchrotron Radiat. 19 (2012) 106. http://dx.doi.org/10.1107/S0909049511039422.

[13] C.J. Sahle, A. Mirone, J. Niskanen, J. Inkinen, M. Krisch, S. Huotari, Planning, performing and analyzing X-ray Raman scattering experiments, J. Synchrotron Radiat. 22 (2015) 400. http://dx.doi.org/10.1039/C1CP20295B.

[14] J. Felsteiner, W. Schlke, Multiple scattering in inelastic X-ray scattering spectroscopy: A Monte-Carlo study, Nucl. Instrum. Methods Phys. Res. B 132 (1997) 1. http://dx.doi.org/10.1016/S0168-583X(97)00400-X.

[15] M.G. Honnicke, L.M. Bianco, S.A. Ceppi, C. Cusatis, X. Huang, Y.Q. Cai, G.E. Stutz, Construction of a quartz spherical analyzer: application to high-resolution analysis of the Ni $K\alpha$ emission spectrum, J. Appl. Crystallogr. 49 (2016) 1443. http://dx.doi.org/10.1107/S1600576716010633.

[16] W. Schülke, H. Nagasawa, Performance of a spherically bent crystal spectrometer for inelastic scattering experiments with synchrotron X-radiation, Nucl. Instrum. Methods Phys. 222 (1984) 203. http://dx.doi.org/10.1016/0167-5087(84)90531-3.

[17] A. Berthold, S. Mourikis, J. Schmitz, W. Schülke, H. Schulte-Schrepping, Performance of a versatile instrumentation for inelastic X-ray scattering spectroscopy (IXSS) with synchrotron radiation, Nucl. Instrum. Methods Phys. Res. Sect. A 317 (1) (1992) 373–382. http://dx.doi.org/10.1016/0168-9002(92)90631-D.

[18] G. Tirao, G. Stutz, C. Cusatis, An inelastic X-ray scattering spectrometer at LNLS, J. Synchrotron Radiat. 11 (4) (2004) 335–342. http://dx.doi.org/10.1107/S0909049504010386.

[19] M. Berger, J. Hubbell, S. Seltzer, J. Chang, J. Coursey, R. Sukumar, D. Zucker, K. Olsen, XCOM: Photon Cross Section Database (version 1.5), National Institute of Standards and Technology, 2010. http://physics.nist.gov/xcom.

[20] J.H. Hubbell, W.J. Veigele, E.A. Briggs, R.T. Brown, D.T. Cromer, R.J. Howerton, Atomic form factors, incoherent scattering functions, and photon scattering cross sections, J. Phys. Chem. Ref. Data 4 (1975) 471–538. http://dx.doi.org/10.1063/1.555523.

[21] D.V. Rao, R. Cesareo, G.E. Gigante, Coherent and incoherent scattering of 14.93, 17.44 and 21.12 keV photons from Al, Cu, Sr, Cd, Ce, Pr, Sm, Pt, Au and Pb, Phys. Scr. 50 (3) (1994) 314. http://stacks.iop.org/1402-4896/50/i=3/a=018.

[22] M. Sánchez del Río, R.J. Dejus, XOP v2.4: recent developments of the x-ray optics software toolkit, Proc. SPIE 8141 (2011) 814115–814115–5.

[23] J. Lindhard, On the Properties of a Gas of Charged Particles, 1954 by J. Lindhard, E. Munksgaard.

[24] G. Onida, L. Reining, A. Rubio, Electronic excitations: Density-functional versus many-body Green's-function approaches, Rev. Modern Phys. 74 (2002) 601–659. http://dx.doi.org/10.1103/RevModPhys.74.601.

[25] S. Huotari, M. Cazzaniga, H.-C. Weissker, T. Pylkkänen, H. Müller, L. Reining, G. Onida, G. Monaco, Dynamical response function in sodium studied by inelastic x-ray scattering spectroscopy, Phys. Rev. B 84 (2011) 075108. http://dx.doi.org/10.1103/PhysRevB.84.075108.

[26] P. Cudazzo, K.O. Ruotsalainen, C.J. Sahle, A. Al-Zein, H. Berger, E. Navarro-Moratalla, S. Huotari, M. Gatti, A. Rubio, High-energy collective electronic excitations in layered transition-metal dichalcogenides, Phys. Rev. B 90 (2014) 125125. http://dx.doi.org/10.1103/PhysRevB.90.125125.

[27] K.O. Ruotsalainen, C.J. Sahle, T. Ritschel, J. Geck, M. Hosoda, C. Bell, Y. Hikita, H.Y. Hwang, T.T. Fister, R.A. Gordon, K. Hämäläinen, M. Hakala, S. Huotari, Inelastic x-ray scattering in heterostructures: Electronic excitations in LaAlO$_3$/SrTiO$_3$, J. Phys.: Condens. Matter 27 (33) (2015) 335501. http://dx.doi.org/10.1088/0953-8984/27/33/335501.

[28] J.A. Soininen, A.L. Ankudinov, J.J. Rehr, Inelastic scattering from core electrons: A multiple scattering approach, Phys. Rev. B 72 (2005) 045136. http://dx.doi.org/10.1103/PhysRevB.72.045136.

[29] J. Kas, K. Jorissen, J. Rehr, Real-space multiple-scattering theory of X-ray spectra, in: X-Ray Absorption and X-Ray Emission Spectroscopy: Theory and Applications, Vol. 1–2, 2015, pp. 51–72. http://dx.doi.org/10.1002/9781118844243.ch3.

[30] J. Vinson, J.J. Rehr, J.J. Kas, E.L. Shirley, Bethe-Salpeter equation calculations of core excitation spectra, Phys. Rev. B 83 (2011) 115106. http://dx.doi.org/10.1103/PhysRevB.83.115106.

[31] K. Gilmore, J. Vinson, E. Shirley, D. Prendergast, C. Pemmaraju, J. Kas, F. Vila, J. Rehr, Efficient implementation of core-excitation Bethe-Salpeter equation calculations, Comput. Phys. Comm. 197 (2015) 109–117. http://dx.doi.org/10.1016/j.cpc.2015.08.014.

[32] G. Hölzer, M. Fritsch, M. Deutsch, J. Härtwig, E. Förster, $K\alpha_{1,2}$ and K$\beta_{1,3}$ X-ray emission lines of the 3d transition metals, Phys. Rev. A 56 (1997) 4554. http://dx.doi.org/10.1103/PhysRevA.56.4554.

[33] M. Deutsch, G. Hölzer, J. Härtwig, J. Wolf, M. Fritsch, E. Förster, $K\alpha$ and $K\beta$ x-ray emission spectra of copper, Phys. Rev. A 51 (1995) 283. http://dx.doi.org/10.1103/PhysRevA.51.283.

[34] Y. Ito, T. Tochio, H. Oohashi, A.M. Vlaicu, Contribution of the [1s3d] shake process to K$\alpha_{1,2}$ spectra in 3d elements, Radiat. Phys. Chem. 75 (2006) 1534. http://dx.doi.org/10.1016/j.radphyschem.2005.10.023.

[35] M. Budnar, A. Mühleisen, M. Hribar, H. Janžekovič, M. Ravnikar, Ž. Šmit, M. Žitnik, K-MM radiative Auger effect in solid Ca, Ti and Cr targets after ionization with 0.7 –1.5 MeV protons, Nucl. Instrum. Methods Phys. Res., Sect. B 63 (1992) 377. http://dx.doi.org/10.1016/0168-583X(92)95208-9.

[36] S.J. Cipolla, K X-ray production cross sections, Kβ/Kα ratios, and radiative Auger ratios for protons impacting low-Z elements, Nucl. Instrum. Methods Phys. Res., Sect. A 422 (1999) 546. http://dx.doi.org/10.1016/S0168-9002(98)01083-3.

[37] H. Enkisch, C. Sternemann, M. Paulus, M. Volmer, W. Schülke, $3d$ spectator hole satellites of the Cu $K\beta_{1,3}$ and $K\beta_{2,5}$ emission spectrum, Phys. Rev. A 70 (2004) 022508. http://dx.doi.org/10.1103/PhysRevA.70.022508.

[38] R.D. Deslattes, E.G. Kessler, P. Indelicato, L. de Billy, E. Lindroth, J. Anton, X-ray transition energies: New approach to a comprehensive evaluation, Rev. Modern Phys. 75 (2003) 35. http://dx.doi.org/10.1103/RevModPhys.75.35.

[39] M.O. Krause, J.H. Oliver, Natural widths of atomic K and L levels, K X-ray lines and several KLL Auger lines, J. Phys. Chem. Ref. Data 8 (2) (1979) 329–338. http://dx.doi.org/10.1063/1.555595.

[40] J.H. Scofield, Exchange corrections of k x-ray emission rates, Phys. Rev. A 9 (1974) 1041–1049. http://dx.doi.org/10.1103/PhysRevA.9.1041. https://link.aps.org/doi/10.1103/PhysRevA.9.1041.

[41] J.H. Scofield, Relativistic hartree-slater values for k and l x-ray emission rates, Atom. Data Nucl. Data Tables 14 (2) (1974) 121–137. http://dx.doi.org/10.1016/S0092-640X(74)80019-7. http://www.sciencedirect.com/science/article/pii/S0092640X74800197.

[42] T. Mukoyama, K. Taniguchi, Atomic excitation as the result of inner-shell vacancy production, Phys. Rev. A 36 (1987) 693–698. http://dx.doi.org/10.1103/PhysRevA.36.693. https://link.aps.org/doi/10.1103/PhysRevA.36.693.